Electrical and dielectric characteristics of molybdenum dioxide nanoparticles for high-performance electrocatalysis

Ibrahim Soliman [a,b], Bijaya Basnet [a], Sulata K. Sahu [b], Dhruba Panthi [c], Yanhai Du [b,*]

[a] College of Aeronautics and Engineering, Kent State University, Kent, OH 44242, USA
[b] Advanced Materials and Liquid Crystal Institute, Kent State University, Kent, OH, 44242, USA
[c] Department of Engineering Technology, Kent State University at Tuscarawas, New Philadelphia, OH, 44663, USA

A B S T R A C T

As an attempt to improve the catalytic processes in different electrochemical systems, molybdenum dioxide nanoparticles were prepared using the hydrothermal method, and their electrical and dielectric properties were investigated. The nanoparticles were polycrystalline with an orthorhombic structure. AC electrical transport properties of the pressed disc were conducted over a temperature range of 303–423 K and a frequency range of 42–5 $\times$ 10^6 Hz. The AC conductivity follows Jonscher's universal dynamic law, and it has been determined that correlated barrier hopping (CBH) is the primary conduction mechanism. The maximum barrier height (W_M) was found to be 0.92 eV. The low activation energy showed that hopping conduction is the dominant mechanism of transporting current. The dielectric parameters were analyzed using both complex permittivity and complex electric modulus, with a focus on how they vary with temperature and frequency. At relatively high temperatures and low frequencies, the dielectric parameters showed a high-frequency dependence. The dielectric modulus showed that relaxation peaks move towards lower frequency when temperature increases. The dielectric relaxation activation energy, ΔE_ω was determined to be 0.31 eV.

1. Introduction

Molybdenum dioxide (MoO$_2$) nanoparticles have gained significant attention as efficient catalysts in various electrocatalytic processes due to their unique electrical and dielectric properties [1,2]. These properties play a crucial role in determining the catalytic performance of MoO$_2$ nanoparticles and can be tailored to enhance their activity and stability. In electrochemical reactions, MoO$_2$ nanoparticles can be used as catalysts to enhance energy conversions and storage technologies such as fuel cells [3,4], water electrolyzers [5], and photoelectrochemical cells [6]. These electrochemical reactions are influenced significantly by the electrical parameters of MoO$_2$ nanoparticles, such as conductivity and charge transport characteristics. The high conductivity of MoO$_2$ nanoparticles enhances the electrocatalytic performance at the catalyst-electrolyte interface, facilitating charge transfer and the redox reaction involved in various electrocatalytic processes [7]. Furthermore, dielectric properties such as dielectric constant and dispersion loss, can provide insight into the behavior of MoO$_2$ nanoparticles in electrocatalysis. At the catalyst-electrolyte interface, the dielectric constant influences polarization effects, affecting the kinetics of reactants adsorption and desorption [8]. Additionally, dielectric spectroscopy sheds light on reaction mechanisms and kinetics by providing a comprehensive understanding of charge storge and

---

* Corresponding author.
  E-mail address: ydu5@kent.edu (Y. Du).

relaxation process [9].

There have been extensive studies on the catalytic efficiency of MoO$_2$ nanoparticles in different electrocatalytic processes. In the oxygen reduction reaction (ORR), MoO$_2$ nanoparticles have displayed a remarkable catalytic activity comparable to traditional platinum-based catalysts, which makes them an attractive candidate and efficient alternative [10]. Furthermore, MoO$_2$ nanoparticles have demonstrated promising performance in hydrogen evolution reactions (HERs) and oxygen evolution reactions (OERs) [11], which are critical in renewable energy and water electrolysis. Optimizing the electrocatalytic performance of MoO$_2$ nanoparticles requires comprehensive understanding of their electrical and dielectric parameters. By utilizing these parameters, a research endeavor can be undertaken to uncover the underlying mechanisms that dictate catalytic activities, improve overall performance, and advance the development of superior electrocatalysts based on MoO$_2$. In this study, we aim to provide valuable insights into the electrical properties and dielectric spectroscopy of MoO$_2$ nanoparticles under a wide range of temperatures. With the comprehensive characterization of these parameters, we are able to establish a deeper understanding of the conduction mechanisms controlling electrical conduction and gain insights into the sources of dielectric losses and defects within MoO$_2$ nanoparticles. This research contributes to a broader knowledge base for the application of MoO$_2$ as electrocatalysts.

2. Experimental techniques

The synthesis of MoO$_2$ nanoparticles was performed using a hydrothermal method, following the procedure established by Ellefson et al. [12]. Molybdenum trioxide (MoO$_3$) dry powder, purchased from Sigma-Aldrich, served as the starting material. To initiate the synthesis, 0.3 g of MoO$_3$ powder was combined with 10 ml of ethylene glycol. Subsequently, 30 ml of distilled water was added to the mixture in a stainless steel-lined autoclave. To ensure a controlled reaction environment, the autoclave was tightly sealed, eliminating any external contaminants. The sealed autoclave was then subjected to a constant temperature of 180 °C for a duration of 12 h, allowing for the hydrothermal reaction to take place. During the hydrothermal process, the elevated temperature and pressure within the autoclave provided favorable conditions for the reduction of MoO$_3$ and the subsequent formation of MoO$_2$ nanoparticles. The interaction between MoO$_3$, ethylene glycol, and water molecules under these conditions facilitated the transformation of the precursor into the desired MoO$_2$ nanoparticles. After the completion of the hydrothermal reaction, the autoclave was allowed to cool down to room temperature. The resulting product, MoO$_2$ nanoparticles, was then collected and air-dried at 50 °C. X-ray diffraction spectroscopy (XRD, Rigaku MiniFlex 600) was used to study the nanostructure of the materials in the 2θ range of 5–90°. The diffraction patterns were collected automatically at a scanning speed 2°min^{-1} within the 2θ range. Scanning electron micrographs of MoO$_2$ were obtained with a field emission scanning electron microscope model-Quanta 250 FEG (FEI). A uniaxial press with a steel holder and 2×10^8 Nm^{-2} of pressure was used to press the nanopowder into a disc shape. The uniaxial press maintains the output disc homogeneity and inhibits the growth of cracks or voids. The produced disc has an approximate thickness of 1.1 mm and an average diameter of 7 mm. The study utilized two layers of silver as ohmic contacts for alternating current Ac measurements on an AlPcCl disc. The measurements were conducted using a Hioki 3532 programmable RLC bridge and included the determination of phase angle, impedance, resistance, and capacitance within a frequency range of 42–5 × 10^6 Hz. Additionally, a technique for calculating the total conductivity σ$_t$ of a substance was employed, utilizing a thermocouple within a temperature range of 303–423 K. The equation used to determine conductivity was σ$_t$ (ω,T) = d/AZ, where A represents the sample's cross-sectional area, d represents the thickness of the disc, and Z is a constant.
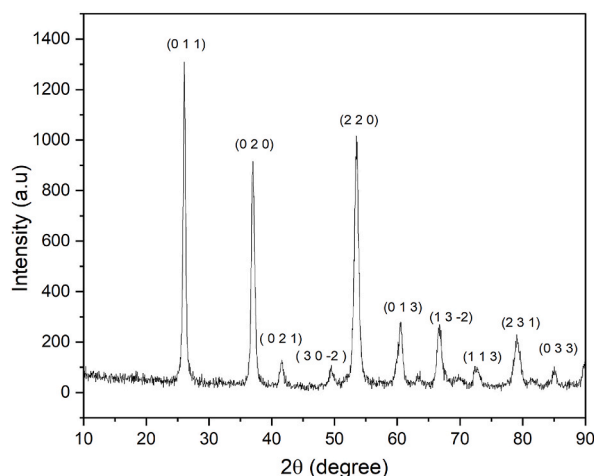

Fig. 1. XRD of MoO$_2$ in powder form.

3. Results and discussion

3.1. Structural characterization

The X-ray diffraction pattern of the MoO$_2$ powder is shown in Fig. 1. The diffraction patterns indicate that the powder material is polycrystalline. The peaks that were observed were matched to JCPDS standards and it was determined that all of the reflections observed can be aligned with an orthorhombic structure (JCPDS No.03-065-5787). The Scherrer formula Eq. 1 was utilized to calculate the full width at half maximum (FWHM) for determining the particle size [13]:

$$D = \frac{0.94\lambda}{\beta \cos(\theta)} \qquad (1)$$

The mean crystallite size (D) was determined by analyzing X-ray diffraction data using the Debye-Scherrer equation. The equation utilizes the wavelength of the copper target (λ), the full width at half maximum (FWHM) of the diffraction peak (β), and the diffraction angle (θ). The average grain size as determined by this XRD analysis was approximately 11.44 nm, which is consistent with the size measurements obtained through scanning electron microscopy, as illustrated in Fig. 2. On the scanning micrograph, nanocrystalline spherical particles of 15–35 nm are distributed almost uniformly across the surface of the sample.

3.2. AC conductivity

The total electrical conductivity $\sigma_t(\omega, T)$ of a material is a measure of its ability to conduct electrical current. It is a function of both frequency (ω) and temperature (T) and can vary greatly depending on the material and the specific conditions under which it is being measured. In the literature, Eq. (2) is an empirical relation that describes the total electrical conductivity over a wide range of frequencies and temperatures [14,15]:

$$\sigma_t(\omega, T) = \sigma_{dc}(T) + \sigma_{ac}(\omega, T) \qquad (2)$$

The total electrical conductivity $\sigma_t(\omega, T)$ of the material can be separated into two components: a frequency-independent DC conductivity $\sigma_{dc}(\omega, T)$, and a frequency-dependent conductivity $\sigma_{ac}(\omega, T)$. The frequency-independent conductivity $\sigma_{dc}(\omega, T)$, can be calculated by extrapolating experimental data at low frequency down to zero value, using Eq. (2). The frequency dependence of $\sigma_{ac}(\omega, T)$ at different temperatures is illustrated in Fig. 3, and can be described mathematically using Eq. (3) [16]:

$$\sigma_{ac}(\omega) = A\omega^s \qquad (3)$$

where ω is the angular frequency, A is a constant that is dependent on temperature, and S is the frequency exponent factor. The frequency exponent S is plotted as a function of temperature, and different theoretical models for AC conductivity can be used to explain the temperature dependence of s and the conduction mechanism. This can provide insight into the electronic properties of the material. As per the electron tunneling model, the frequency exponent s is not depending on the temperature but on frequency. For some forms of tunneling, such as large polaron tunneling, s is seen to decrease to a certain temperature range and then increase. This is observed in Fig. 4 where the value of s reduces as temperature increases. This pattern is explained by the correlated barrier hopping theory, where the charge carriers move between sites by jumping over potential barriers between them. This mechanism states that the frequency exponent s decreases as temperature increases. Eq. (4) represents the AC conductivity in this model is represented as follows [17]:
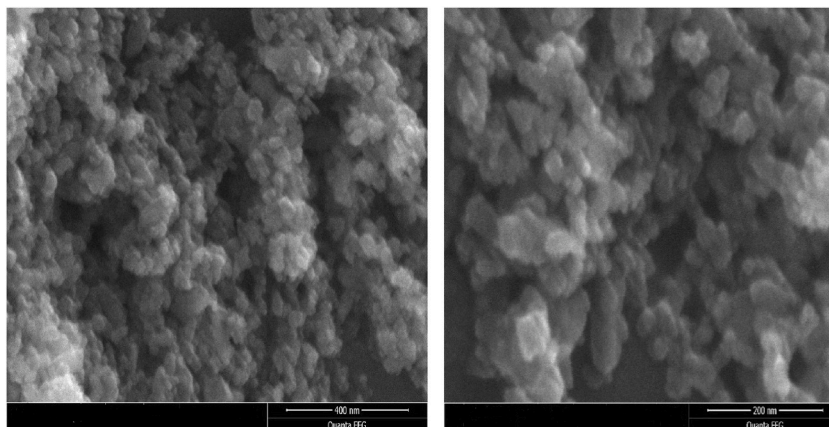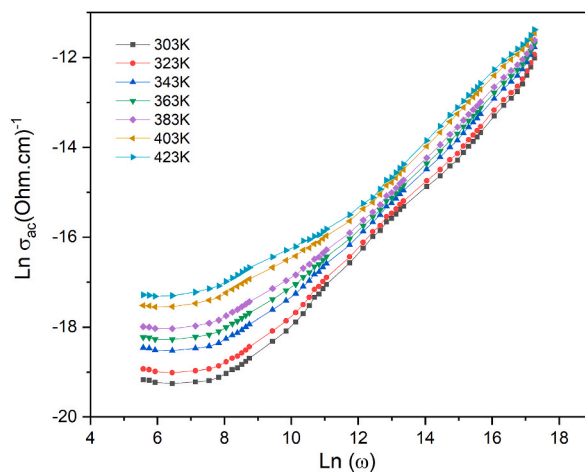

Fig. 2. SEM micrographs of MoO$_2$ surface.

Fig. 3. Frequency dependence of σ_{ac} for MoO_2 at different temperatures.
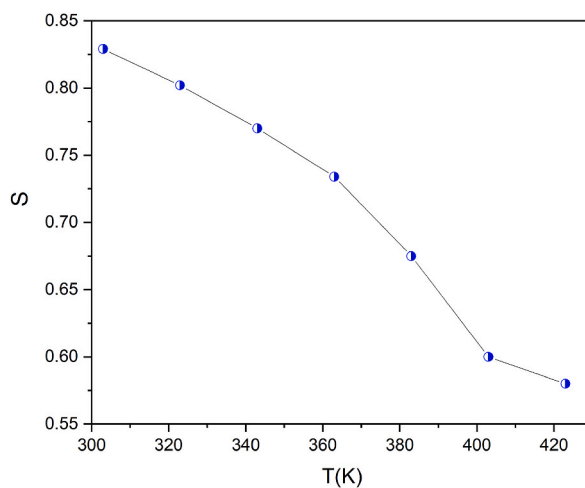

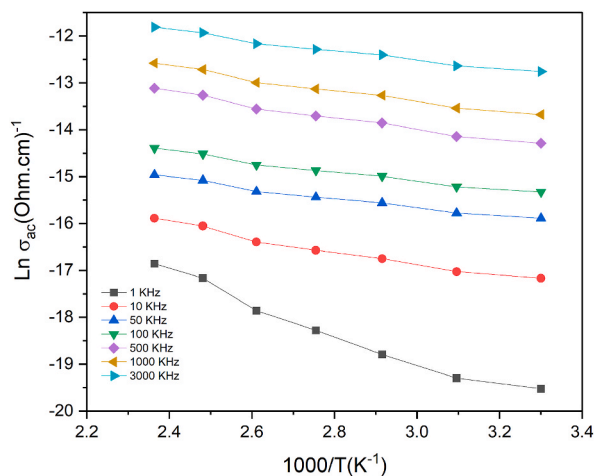**Fig. 4.** Temperature dependence of power exponent (s).

Fig. 5. Temperature dependence of σ_{ac} at different frequencies.

$$\sigma_{ac}(\omega) = \frac{\pi^2 [N(E_F)]^2 \varepsilon}{24} \left(\frac{8e^2}{\varepsilon W_M}\right)^6 \frac{\omega^s}{\tau_0^{1-s}} \tag{4}$$

The model includes several parameters, including the density of localized states N (E_F), dielectric constant (ε), electronic charge (e), maximum barrier height for electron hopping W_M, and effective relaxation time τ_o. Additionally, the frequency exponent (s) is also provided [17]:

$$s = 1 - \frac{6K_B T}{[W_M + K_B T \ln(\omega \tau_o)]} \tag{5}$$

The initial approximation results in a simple formula for the s value, which is given by Eq. (6) [18]:

$$s = 1 - \left(6K_-(B)\ T\ /\ W_M\right) \tag{6}$$

The value of W_M was determined to be 0.92 eV when the temperature is set to 303 K and using the Boltzmann constant K_B. Fig. 5 shows how σ_{ac} changes with temperature. The temperature causes the ln (σ_{ac}) to increase linearly at different frequencies, meaning that the ac conductivity is affected by temperature through different localized states of the gap [19]. It has been determined that the dependence of σ_{ac} on temperature determined by the following Eq. (7) [16].

$$\sigma_{ac} = \sigma_0 \exp(-\Delta E_{ac}\ /\ K_B T) \tag{7}$$

Where σ_o is the pre-exponential constant and ΔE_{ac} is the activation energy of Ac conduction. The slopes of the lines in Fig. 5 are used to calculate the activation energy of AC conduction at different frequencies. Fig. 6 shows the relationship between frequency and ΔE_{ac}. As the frequency increases, ΔE_{ac} tends to decrease. The current transport is mainly driven by hopping conduction, which is characterized by low activation energy. Thus, when the frequency increases, the electronic jumps between the localized states also increase [20].

3.3. Dielectric studies

The complex dielectric permittivity of a material, $\varepsilon^*(\omega) = \varepsilon_1 (\omega) + \varepsilon_2(\omega)$, is composed of two parts: the dielectric constant (ε_1) which is the real component, and the dielectric loss (ε_2) which is the imaginary component [19–21]. The ratio between these two parts is called the loss tangent (tan $\delta = \varepsilon_2/ \varepsilon_1$) [21]. Studying the frequency dependence of the dielectric constant is shown in Fig. 7. The results show that at a constant temperature, the dielectric constant decreases as the frequency increases. This means that the material's ability to store electrical energy in an electric field decreases as the frequency increases. The decrease in dielectric constant with increasing frequency is caused by the dipoles' inability to rotate quickly and follow the applied field at high frequencies [21]. Fig. 8 illustrates the relationship between the dielectric constant represented by ε_1, and temperature at constant frequencies. The figure shows that as the temperature increases, the dielectric constant also increases. This implies that the material's ability to store electrical energy in an electric field increases as the temperature increases. This behavior can be attributed to the increase in kinetic energy of the material's electrons as the temperature rises, which allows them to move more freely and align better with the electric field. Additionally, at higher temperatures, the material's ions vibrate more, leading to increased polarizability of the material, and further contributing to the increase in dielectric constant [22]. Figs. 9 and 10 show how the dielectric loss, ε_2, changes with frequency and temperature respectively. The data in the figures reveal that the values of ε_2 follow a similar pattern as ε_1. The main source of dielectric loss is dipole loss which occurs due to the rotational movement of the dipoles in the material [22]. Additionally, as the temperature increases, the movement of the dipoles and free charge carriers in the material increases, leading to an increase in the losses due to
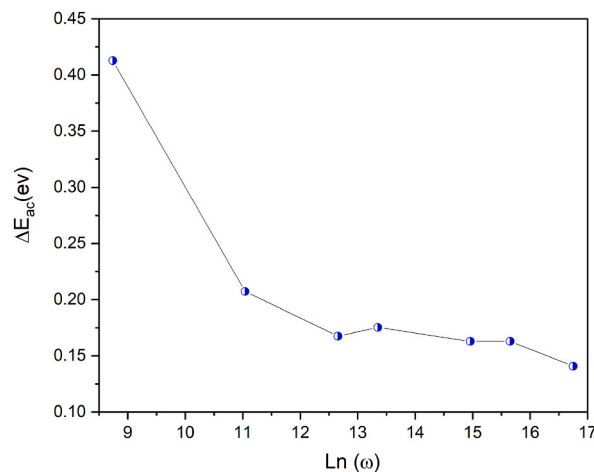

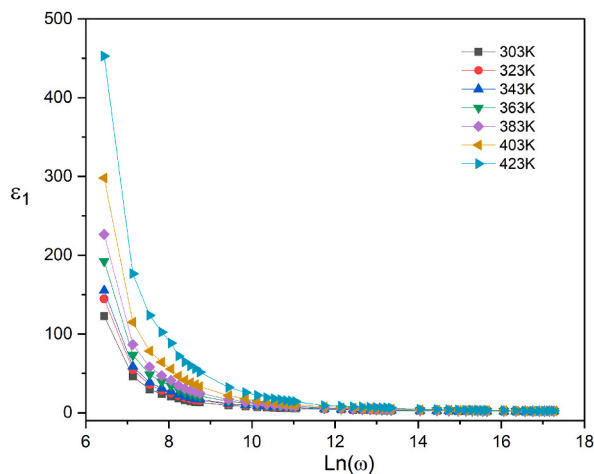**Fig. 6.** Frequency dependence of the AC activation energy for MoO_2.

Fig. 7. Frequency dependence of dielectric constant, ε_1, at different temperatures.
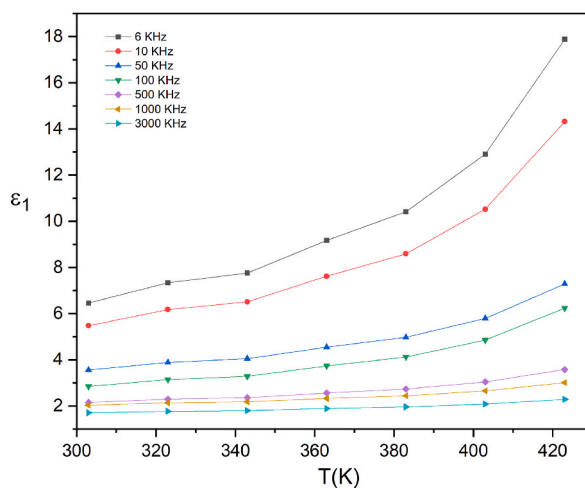

Fig. 8. Temperature dependence of dielectric constant, ε_1, at different frequencies.
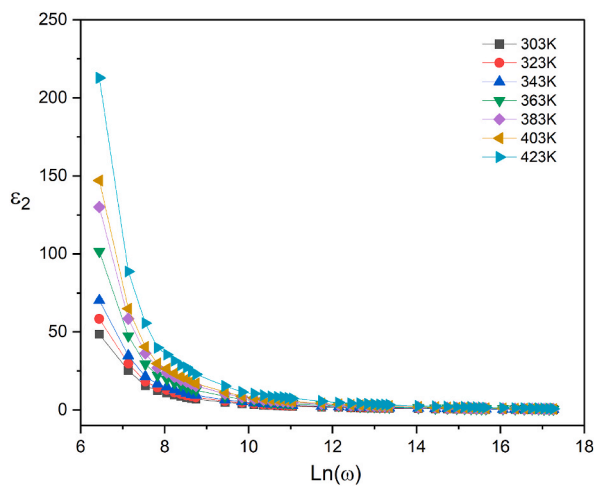

Fig. 9. Frequency dependence of dielectric constant, ε_2, at different temperatures.
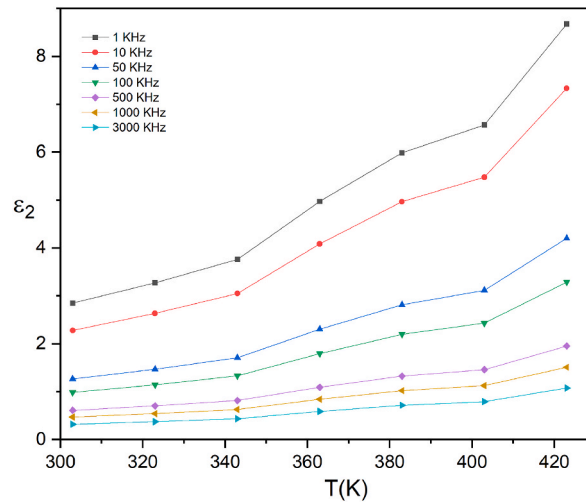
Fig. 10. Temperature dependence of dielectric constant, ε_2, at different frequencies.

dipole movement and conduction [22]. Dielectric modulus, also known as electric modulus, M*, can be used as an alternative way to describe the electrical properties of materials. M* gives an insight into how a material responds to an applied electric field and the relationship between electric displacement and field strength and helps to distinguish between the material's general electrical conductivity and localized dielectric properties, like dipole reorientation. The real and imaginary dielectric moduli, represented by M' and M'', respectively, were calculated using the standard formulas as shown in Eqs. (8)–(10) [23]:

$$M^*(\omega) = 1 \,/\, \varepsilon^*(\omega) = M' + iM'' \tag{8}$$

$$M'(\omega) = \varepsilon_1 \,/\, \left[(\varepsilon_1)^2 + (\varepsilon_2)^2\right] \tag{9}$$

$$M''(\omega) = \varepsilon_2 \,/\, \left[(\varepsilon_1)^2 + (\varepsilon_2)^2\right] \tag{10}$$

The values of $M''(\omega)$ as depicted is shown in Fig. 11. In the low-frequency range, values tend to zero. The presence of a low-frequency tail may be a result of the high capacitance associated with the electrodes [24]. A well-defined peak becomes more pronounced as the temperature increases. This is accompanied by a systematic shift of the maximum peak position towards higher frequencies, implying that the relaxation rate of the process increases with increasing temperature [21]. The area below the peak maximum in frequency is significant in figuring out the range where the charge carriers are capable of moving over long distances. The characteristic relaxation times can be calculated by measuring the inverse frequency of maximum positions, with the equation $\tau_m = \omega_m^{-1}$ [25]. By utilizing the Arrhenius relationship using Eq. (11), the temperature dependence of the characteristic relaxation time can be identified, as depicted in Fig. 12.
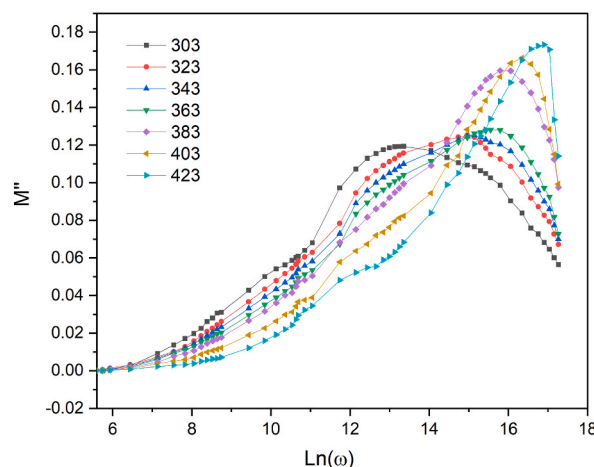

Fig. 11. Frequency dependence of electric modulus, M'', at different temperatures.
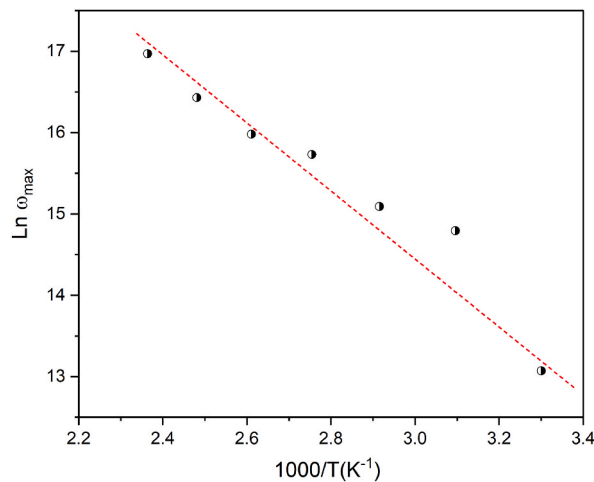
Fig. 12. Variation of ln ω_{max} vs. 1000/T.

$$\omega_m = \omega_o \exp(-\Delta E_\omega / K_B T) \tag{11}$$

where ω_o is the pre-exponent factor, ΔE_ω is the activation energy for dielectric relaxation. the value of ΔE_ω was determined to be approximately 0.31 eV. The graph in Fig. 13 depicts the plots between M''/M''_{max} vs. ln (ω/ω_m) at different temperatures, where M''_{max} is the maximum value of the imaginary component of the electric modulus. The fact that the curves for all temperatures overlap shows that all the dynamic processes are relatively independent of temperature [26].

4. Conclusion

A simple hydrothermal synthesis method was used to synthesize MoO_2 nanoparticles. Microstructural, morphological, electrical, and dielectric properties of the catalyst material were conducted. The XRD and SEM results confirmed the polycrystalline nature of the prepared samples. The frequency dependence of σ_{ac} at different temperatures was studied to determine the conduction mechanism. Correlated barrier hopping was found to be the dominant conduction mechanism where carriers hop between conduction sites over a potential barrier separating them. The temperature dependence of σ_{ac} at different frequencies was investigated to determine the activation energy ΔE_{ac}, which was found to be decreased with increasing frequency. The dielectric properties were studied as a function of frequency and temperature. The dielectric properties were decreasing with increasing frequency, but at relatively high temperatures and low frequencies, the dielectric constant exhibited high-frequency dependence. As a result, the polarizability factor of ϵ_1 and ϵ_2 is a result of relaxation polarization (interfacial and orientational) and deformational polarization (ionic and electronic). The electric modulus M* was studied to determine dielectric relaxation, which was found to be 0.31 eV. Besides, it explained how dynamic processes depend on temperature.
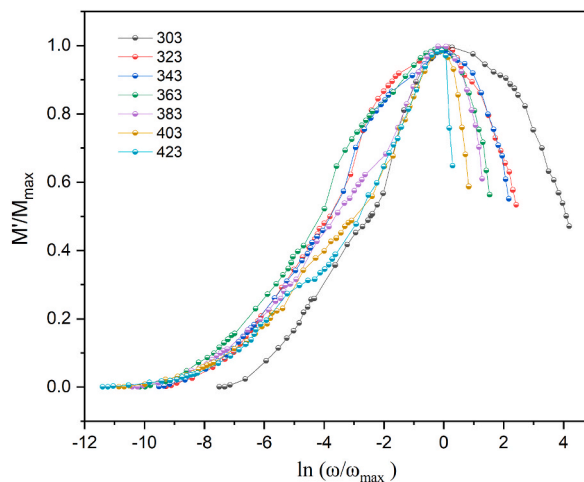

Fig. 13. Normalized plots of M''/M''_{max} vs. ln (ω/ω_{max}) at different temperatures.

Author contribution statement

Ibrahim Soliman: Conceived and designed the experiments; Performed the experiments; Analyzed and interpreted the data; Wrote the paper.

Bijaya Basnet: Conceived and designed the experiments; Performed the experiments; Analyzed and interpreted the data; Contributed reagents, materials, analysis tools or data.

Sulata K. Sahu, Dhruba Panthi: Contributed reagents, materials, analysis tools or data.

Yanhai Du: Conceived and designed the experiments; Analyzed and interpreted the data; Contributed reagents, materials, analysis tools or data; Wrote the paper.

Data availability statement

Data will be made available on request.

Declaration of competing interest

We do not have either financial interest or personal relationship which may be considered as potential competing interest.

References

[1] Z. Zhuang, J. Huang, Y. Li, L. Zhou, L. Mai, Chemelectrochem 6 (2019) 3570–3589.
[2] I.A. De Castro, R.S. Datta, J.Z. Ou, A. Castellanos-Gomez, S. Sriram, T. Daeneke, K. Kalantar-zadeh, Adv. Mater. 29 (2017), 1701619.
[3] X. Yang, D. Panthi, N. Hedayat, T. He, F. Chen, W. Guan, Y. Du, Electrochem. Commun. 86 (2018) 126–129.
[4] S. Karthick, K. Haribabu, Fuel 275 (2020), 117994.
[5] A.Y. Faid, A.O. Barnett, F. Seland, S. Sunde, ACS Appl. Energy Mater. 4 (2021) 3327–3340.
[6] X. Wu, J. Li, Y. Li, Z. Wen, Chem. Eng. J. 409 (2021), 128161.
[7] X. Chen, H. Sun, P. Liang, X. Zhang, X. Huang, J. Power Sources 324 (2016) 79–85.
[8] D. Saha, P. Kruse, J. Electrochem. Soc. 167 (2020), 126517.
[9] E. Zhou, C. Wang, Q. Zhao, Z. Li, M. Shao, X. Deng, X. Liu, X. Xu, Ceram. Int. 42 (2016) 2198–2203.
[10] L. Yang, J. Yu, Z. Wei, G. Li, L. Cao, W. Zhou, S. Chen, Nano Energy 41 (2017) 772–779.
[11] J. Chen, X. Qi, C. Liu, J. Zeng, T. Liang, ACS Appl. Mater. Interfaces 12 (2020) 51418–51427.
[12] A. V Shishkin, M.Y. Sokol, A.A. Vostrikov, Thermophys. Aeromechanics 20 (2013) 647–650.
[13] M.M. El-Nahass, H.S. Soliman, B.A. Khalifa, I.M. Soliman, Mater. Sci. Semicond. Process. 38 (2015).
[14] A.K. Jonscher, Nature 267 (1977) 673–679.
[15] K. Shimakawa, S.R. Elliott, Phys. Rev. B 38 (1988), 12479.
[16] I.M. Soliman, M.M. El-Nahass, Y. Mansour, Solid State Commun. 225 (2016).
[17] S.R. Elliott, Philos. Mag. A 36 (1977) 1291–1304.
[18] S.A. Mansour, I.S. Yahia, F. Yakuphanoglu, Dye. Pigment. 87 (2010) 144–148.
[19] F. Yakuphanoglu, Y. Aydogdu, U. Schatzschneider, E. Rentschler, Solid State Commun. 128 (2003) 63–67.
[20] H.S. Soliman, M. Ibrahim, M.A.M. El-Mansy, S.M. Atef, Opt. Mater. 72 (2017) 122–129.
[21] M.M. El-Nahass, H.A.M. Ali, Solid State Commun. 152 (2012) 1084–1088.
[22] N.A. Hegab, M.A. Afifi, H.E. Atyia, A.S. Farid, J. Alloys Compd. 477 (2009) 925–930.
[23] J. Wei, L. Zhu, Prog. Polym. Sci. 106 (2020), 101254.
[24] S.B. Aziz, O.G. Abdullah, S.R. Saeed, H.M. Ahmed, Int. J. Electrochem. Sci. 13 (2018) 3812–3826.
[25] M.H. Buraidah, L.P. Teo, S.R. Majid, A.K. Arof, Phys. B Condens. Matter 404 (2009) 1373–1379.
[26] M. Jebli, M.A. Albedah, J. Dhahri, M. Ben Henda, M.L. Bouazizi, H. Belmabrouk, J. Inorg. Organomet. Polym. Mater. (2022) 1–20.